J. Fluid Mech. (1993), *vol.* 249, *pp.* 35–57

Structure of bubble plumes in linearly stratified environments

By TAKASHI ASAEDA† AND JÖRG IMBERGER

Centre for Water Research, The University of Western Australia, Nedlands, 6009, Western Australia

(Received 1 May 1989 and in revised form 6 October 1992)

Bubble plumes in a linearly stratified ambient fluid are studied. Four well-defined flow regions were observed: an upward-moving bubble core, an inner plume consisting of a mixture of bubbles and relatively dense fluid, an annular downdraught and beyond that a horizontal intrusion flow. Depending on the gas flow rate with respect to the stratification, three types of intrusions were documented. At large gas flow rates a single intrusion was observed. As the gas flow rate was decreased, the buoyancy flux was insufficient to carry the lower fluid to the surface and a stack of intrusions were formed. At very low gas flow rates the intrusions became unsteady. The transition between these three regimes was observed to occur at critical values of the parameters $N^3H^4/(Q_B g)$, $Q_B g/(4\pi\alpha^2 u_s^3 H)$, and H/H_T, where N is the buoyancy frequency, H is the water depth, H_T is equal to $H+H_A$, H_A being the atmospheric pressure head, Q_B is the gas flow rate at the bottom, g the acceleration due to gravity, α the entrainment coefficient and u_s the differential between the bubble and the average water velocity commonly called the slip velocity. The height between intrusions was found to scale with the Ozmidov length $(Q_B g/N^3)^{\frac{1}{4}}$, the plunge point entrainment with the inner plume volume flux $(Q_0 g)^{\frac{3}{4}}N^{-\frac{5}{4}}$ and the radial distance to the plunge point with $(Q_0 g/N^3)^{\frac{3}{4}}$, where Q_0 is the gas flow rate at the free surface.

These results were used to construct a double annular plume model which was used to investigate the efficiency of conversion of the input bubble energy to potential energy of the stratification; the efficiency was found to first increase, reach a maximum, then decrease with decreasing gas flow rate. This agreed well with the results from the laboratory experiments.

1. Introduction

Bubble plumes have been used for a variety of purposes: bubble breakwaters, antifreeze measures in harbours, destratification of lakes and as bubble curtains for the containment of oil spills.

Previous work was concentrated almost exclusively on plumes in homogeneous water (Bulson 1961; Kobus 1968; Wilkinson 1979; Milgram 1983; Tacke *et al.* 1985; Sun & Faeth 1986; Cheung & Epstein 1987). These papers describe various aspects of the mean flow characteristics of the induced plumes including the velocity distribution, entrainment coefficient and the bubble slip velocity. Many of these papers followed the early work of Ditmars & Cederwall (1974) who presented an integral model of such plumes which allowed for a finite gas fraction as well as a non-

† Present address: Department of Civil Engineering, Saitama University, Urawa, Saitama, Japan.

zero bubble slip velocity, the latter reducing the available buoyancy force for a given gas flow rate.

McDougall (1978) and Hussain & Narang (1984) generalized the integral model to include a stratified ambient fluid. For a strongly stratified fluid McDougall (1978) showed, both from the integral model results and from experimental evidence, that the bubble plume forms a core of rising fluid which is surrounded by an annular downdraught; horizontal intrusions into the ambient fluid formed at regular intervals, drawing mixed fluid from the downdraught. Similarly, one strong intrusion was observed by Goosens & Van Pagee (1977), Kranenburg (1979), and Zic, Stephan & Ellis (1992). Recently, Baines & Leitch (1992) reported observations at very weak gas flows and for very strongly stratified ambient fluids. For such conditions, their experimental results showed that the steady intrusions observed by McDougall (1978) were replaced by unsteady collapsing eddies which had the appearance of commencing intrusions, but which quickly lost their momentum because of a lack of continuity of source fluid; the downdraught in the outer annulus appeared to be unsteady.

The aim of the present study was to elucidate the behaviour of bubble plumes in a stratified ambient fluid under a wide range of flow conditions, to explain the observed changes in the flow behaviour and, finally, to describe the variation in the efficiency of energy conversion. The influence of bubble surface tension or bubble size will not be discussed here. In general the gas flow rates and bubble sizes were such as to form bubble plumes with well-defined bubble cores (Wilkinson 1979).

2. Experimental procedures

These experiments were carried out in a 100×100 cm glass tank containing water to a depth of 75 cm. Air bubbles were released from two types of bubble makers, one consisting of a hollow tube 2.4 cm in diameter with a circular top made of a uniform porous ceramic material, the other being a fine nozzle. Bubbles were released from the ceramic disc through an area of approximately 20–50 mm^2 depending on the flow rate. The bubble maker was connected by a tube to a compressor and was positioned at the centre of the tank so that its top was 15 cm above the bottom of the tank. Attached to the middle of the air feeder tube was a relief tube, the outer end of which was submerged to a depth of 0.5–1.0 m in a second tank. The gas flow rate was adjusted by changing the tension of a tube clamp and by altering the difference in water level between the main and relief tanks. The pressure fluctuations associated with bubbling were small compared to the total pressure drop; however, the gas flow rate from the bubble maker changed gradually during the first hour after the start of bubbling. Hence, measurements were initiated only after at least three hours of bubbling, during which time the bubble maker was isolated from the tank by placing a thin tube over the bubble stream. This prevented any mixing of the stratification. The gas flow rates were measured before and after each run; the difference was mostly less than 2% of the total flow rate.

The linear stratification was created by the two-tank method and salt was used as the stratifying agent; a Head conductivity probe (Head 1983) was used to measure the conductivity of the water. Vertical profiles were taken so that a conductivity reading was obtained approximately every 2 mm.

The structure of the instantaneous flow field was visualized by shadowgraph, and the net spread of fluid exiting from the plume was obtained by injecting different coloured dyes, at various times, through a small tube mounted 3 cm above the

bubble maker. Since the light source for the shadowgraph was only 10 m away from the tank, a parallax correction was included; the actual positions and scales in the shadowgraph images were calculated from scales drawn on both the front and back walls of the tank.

The rising velocity of bubbles was calculated from the length of traces, on photographic images, of illuminated bubbles in photographs taken with a certain exposure time. After each run, the rise velocity of bubbles in still water was measured by the following techniques: bubbles were fanned away from the plume so as to distribute them over a wide area throughout the tank to remove the interaction of bubbles and eliminate the plume rise velocity. After the turbulence caused by fanning had dissipated and the bubbles began to rise steadily, an estimate of the slip velocity could be made. This was used in calculating the parameter M_{H} defined later. Since the bubbles were considerably smaller than the equilibrium size for that depth of water, the fanning did not cause any bubble breakup.

The maximum bubble size was generally less than 2.0 mm for the ceramic bubbler, generally smaller than those made by the nozzle bubbler which yielded bubbles with a diameter of about 4 mm; the tank was of insufficient depth to allow bubbles to coalesce or expand and the bubble size remained essentially constant over the depth of the tank. Hence, the bubble size and the gas flow rate were a function only of the pressure in the air feeder tube; for the ceramic bubbler at high pressure a large number of pores in the ceramic top were opened by the gas, and the velocity of the gas passing through the ceramic increased. However, since there was less distance between open pores at such high pressure, more bubbles merged with each other and, as a result, the size of bubbles generally increased with pressure.

The experimental conditions are summarized in table 1.

3. Flow patterns

As in the case of the homogeneous water, the initiation of bubbles in a linear stratification caused the surrounding water to be entrained and carried up with the bubble stream. However, at some level, the increased negative buoyancy of the entrained water led to detrainment of water outwards, away from the upward moving plume. The detrained water formed an annular downward flow immediately outside the inner upward-moving plume. This flow continued to plunge downwards, entraining ambient fluid and shedding fluid into the inner plume, until it reached a level of neutral buoyancy, where a horizontal intrusion formed. After detraining some fraction of the heavier water, the water in the bubble core continued rising upwards and the process repeated itself until the bubble plume reached the surface. At the surface the flow spread outwards, decreasing in velocity with distance. At a certain radius blocking by the ambient stratification arrested the horizontal momentum of the radial surface flow and the negative buoyancy caused it to plunge. At that point the heavier water initiated a negatively buoyant plume which again entrained ambient surface water as it moved downwards. The falling plume propagated downwards to a level of neutral buoyancy where it formed a further intrusion; the general appearance was similar to a mushroom. For large gas flow rates, the first detrainment point was also the surface outflow (type 1). However, for smaller gas flows, several stable intrusions were found between the first and the highest intrusions. Very small gas flow rates produced a pattern similar to that documented by Baines & Leitch (1992) with no steady intrusions being observed (type 3).

Run	Q_0 (m^3/s) $\times 10^{-6}$	N^2 ($1/s^2$)	H (m)	P_{HT} $\times 10^6$	P_N	M_H[a] $\times 10^{-2}$	R_s (m) $\times 10^{-2}$	Q_{se} (m^3/s) $\times 10^{-6}$	η (%)	$\frac{z_u}{H}$[b]	$\frac{z_l}{H}$[c]	Type	$\frac{z_i}{H}$[d]
Ceramic bubbler experiments													
C1	0.645	0.170	0.60	159	1522	22.5	7.3	45	12.7	0.91	0.22	2	0.84 0.40
C2	2.14	0.075	0.60	14.1	139	9.36	26.8	240	7.7	0.85	0.52	1	0.78
C3	0.155	0.114	0.60	365	3477	11.3	7.9	—	—	0.95	0.16	3	—
C4	0.507	0.122	0.60	124	1177	17.6	7.6	—	12.5	0.92	0.24	2	0.84 0.47
C5	0.0332	0.0627	0.60	695	6622	9.18	6.1	7.43	11.7	0.95	0.13	3	—
C6	4.08	0.141	0.60	19.1	182	9.18	—	—	9.2	—	—	1	—
S1	0.467	0.179	0.40	216	440	30.2	6.8	—	11.0	0.89	0.27	1	0.77
S2	0.740	0.122	0.36	75.7	102	30.8	11.8	97.2	—	0.88	0.49	1	0.80
S3	2.0	0.0875	0.38	17.1	28.5	17.0	21.0	—	6.6	0.88	0.58	1	0.77
CC	0.60	0.0880	0.58	63.4	531	21.6	—	—	—	0.95	0.31	2	0.85 0.55
B2	0.0443	0.165	0.56	218	1601	24.8	6.7	29.6	—	—	—	2	—
B3	12.8	0.139	0.56	5.84	42.8	14.0	—	—	—	—	—	1	—
B4	0.082	0.139	0.56	912	6690	8.06	5.6	12.0	—	—	—	3	—
B5	0.025	0.161	0.56	3730	27360	—	10.4	—	—	—	—	2	—
B7	2.20	0.301	0.56	108	795	—	—	61.8	—	—	—	—	—
B8	1.28	0.310	0.56	195	1427	14.2	—	—	—	—	—	2	—
ST1	0.584	0.179	0.51	183	954	23.7	—	—	—	—	—	2	—
ST2	2.20	0.225	0.56	69.9	505	9.60	—	—	—	—	—	1	—
ST3	5.31	0.234	0.51	30.1	156	13.0	—	191	—	—	—	1	—

Nozzle bubbler experiments													
L1	4.33	0.092	0.54	9.22	60.2	6.20	—	—	5.6	—	—	1	—
L2	1.04	0.283	0.55	209	1466	1.50	6.1	—	—	0.85	0.06	3	—
L3	0.978	0.319	0.57	267	2064	1.34	5.8	—	5.0	1.0	0.06	3	—
L4	8.24	0.130	0.56	8.22	62.0	11.4	23.7	—	6.6	0.90	0.54	1	0.81
L5	3.27	0.151	0.57	26.0	207	4.46	13.3	—	8.5	0.91	0.33	1	0.79
L6	0.439	0.218	0.56	334	2420	0.61	—	—	5.1	1.0	0.00	3	—
L21	1.99	0.304	0.56	121	891	0.27	9.5	—	7.0	—	—	3	—
L22	3.28	0.413	0.57	117	921	4.46	11.4	—	—	—	—	3	—
L23	5.78	0.333	0.57	48.1	378	11.5	15.9	6.8	—	—	—	1	—
L31	1.43	0.437	0.53	287	1711	2.11	5.9	8.8	—	—	—	3	—
Maruyama Reservoir experiments													
							($\times 10^2$)	($\times 10^6$)					
M1	2550	0.00107	20	0.00345	663	16	5	1.27	—	—	—	2	—
M2	6200	0.00107	20	0.00142	272	38	6	0.967	—	—	—	1	—
M3	2550	0.00107	30	0.0144	4471	7.7	—	—	—	—	—	m[e]	—
M4	6200	0.00107	30	0.00593	1838	19	—	—	—	—	—	2	—

[a] α was chosen as 0.083.
[b] The upper edge of the highest intrusion.
[c] The lower edge of the lowest intrusion.
[d] Intrusion positions.
[e] Multiple intrusions (the number is unknown).

TABLE 1. Experimental conditions

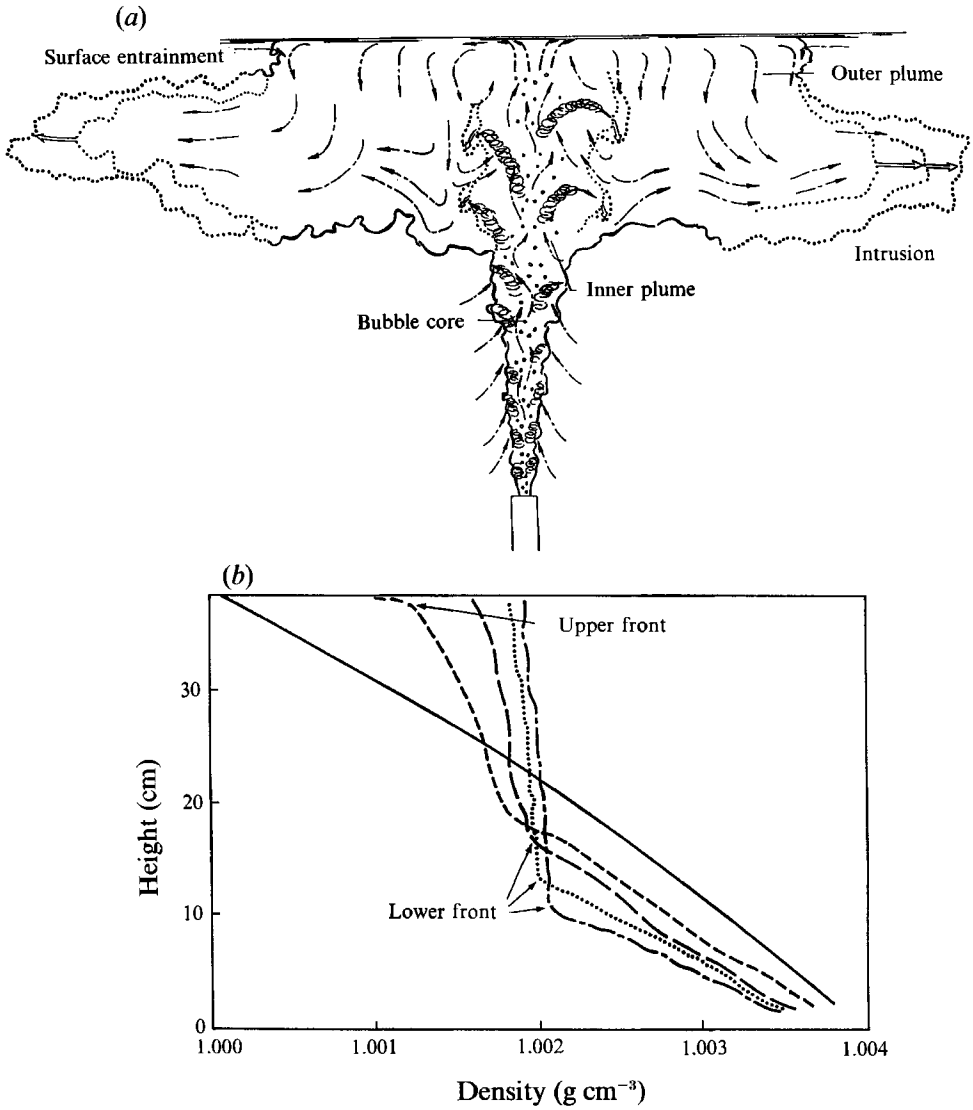

FIGURE 1. (*a*) Sketch of a typical flow pattern for high gas flow rates and weak stratification (type 1). Solid spirals show strong eddies; solid arrows, eddy motions; dash-dotted arrows, fluid motion, and hollow arrows, front motions. (*b*) Typical changes in the ambient density profiles for this case: ——, the initial distribution; - - - - -, $t = 270$ s; – – –, 510 s; · · · · ·, 870 s; – · – · –, 1050 s. $Q_0 = 2.0 \times 10^{-6}$ m^3 s^{-1}; $N^2 = 0.0876$ s^{-2}, and $H = 0.38$ m. The measurement was carried out midway between the plunge point and the sidewall. The upper front was almost at the water surface by the time 270 s had elapsed.

Hereafter, the area in the plume containing the bulk of the air bubbles will be called the 'bubble core', and the upward moving fluid the 'inner plume' and the annular downdraught the 'outer plume'.

3.1. *Type* 1 (*large gas flow rate, weak stratification*)

The flow pattern when the gas flow was relatively high or the stratification was relatively weak is illustrated in figure 1 (*a*). This was similar to that formed by a

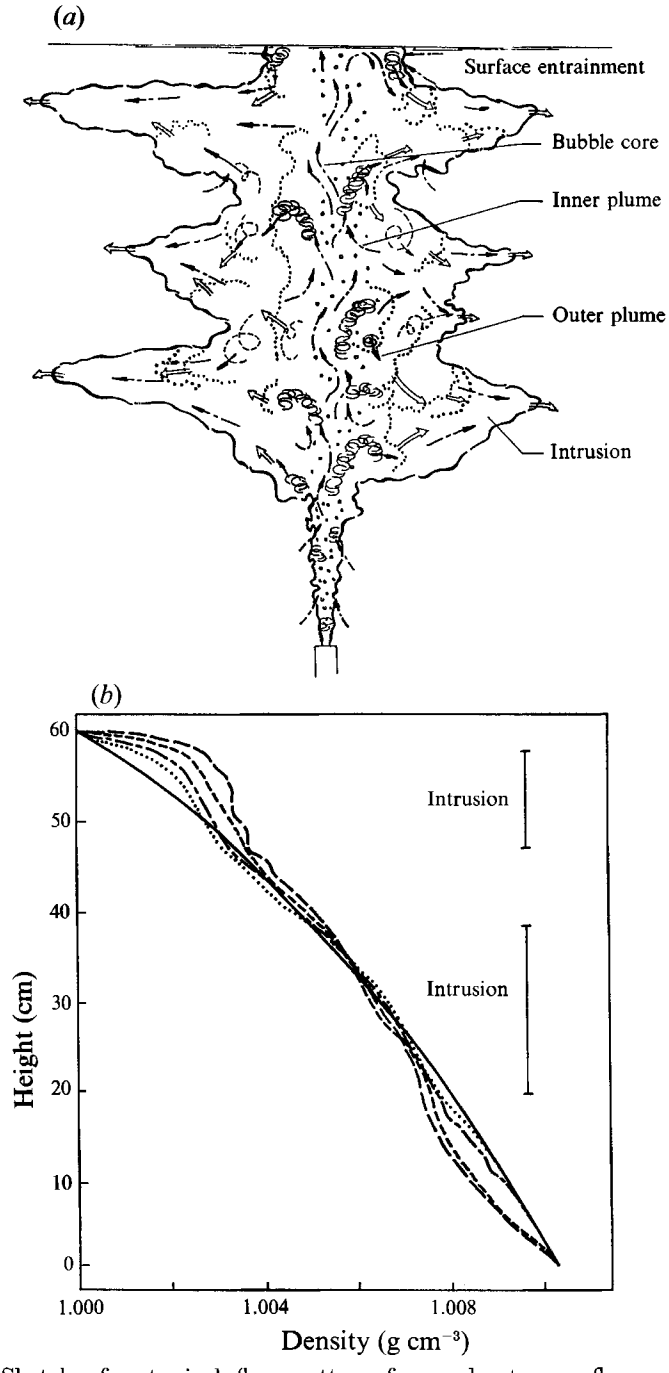

FIGURE 2. (*a*) Sketch of a typical flow pattern for moderate gas flow rate and moderate stratification (type 2). Solid spirals show strong eddies; dashed spirals, weak eddies; solid arrows, eddy motions; dash-dotted arrows, fluid motion; and hollow arrows, front motions. (*b*) Change in density profiles for this case (a two-intrusion example): ——, the initial distribution; · · · · ·, t = 312 s; – – – –, 512 s; – – –, 892 s; – – –, 1200 s. $Q_0 = 6.45 \times 10^{-7}$ m^3 s^{-1}; $N^2 = 0.170$ s^{-2}, and H = 0.60 m. Vertical bars show the positions of intrusions.

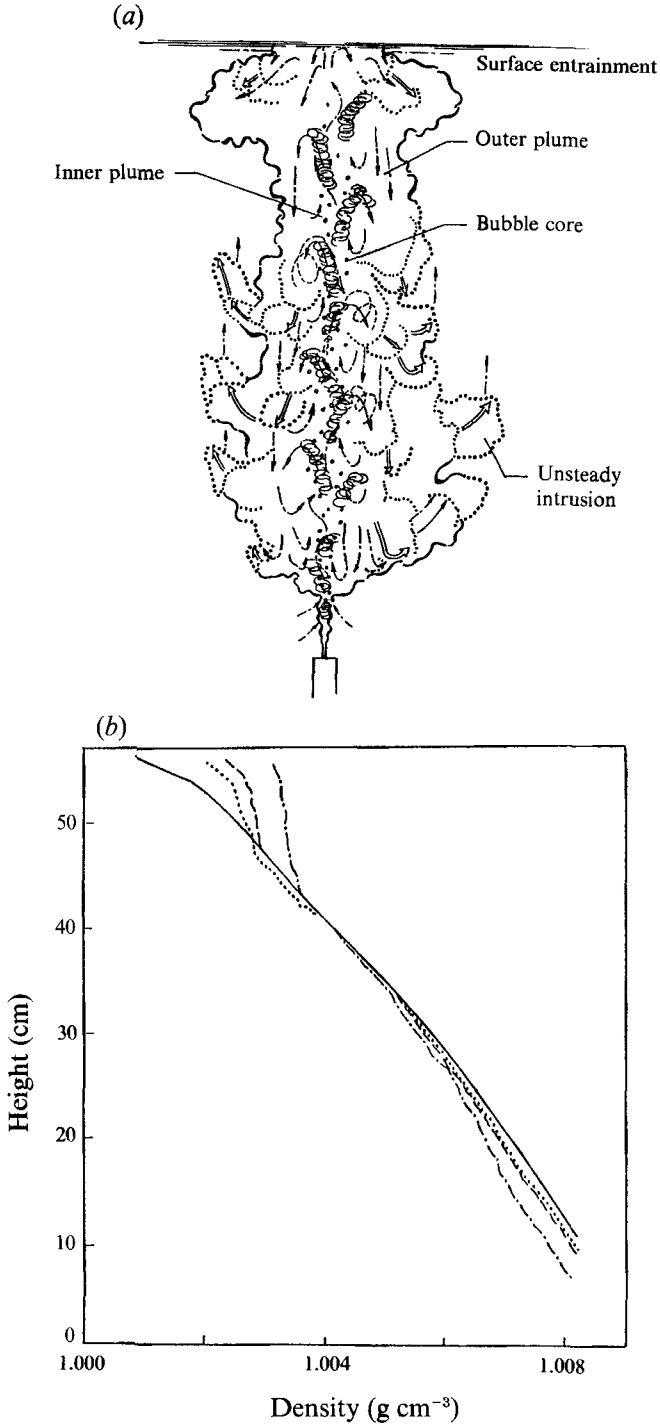

FIGURE 3. (*a*) Sketch of a typical flow pattern for low gas flow rates and strong stratification (type 3). Solid spirals show strong eddies; dashed spirals, weak eddies; solid arrows, eddy motions; dash-dotted arrows, fluid motion; and hollow arrows, front motions. (*b*) Changes in the ambient density profiles for this case: ——, the initial distribution; · · · · ·, t = 900 s; - - - -, 2160 s; —·—·—·—, 7260 s. $Q_0 = 8.20 \times 10^{-8}$ m^3 s^{-1}, $N^2 = 0.139$ s^{-2}, and $H = 0.56$ m.

simple plume impinging on the free surface (strong buoyancy flux). Along the outer edge of the inner plume, small eddies formed and rose up, rotating strongly like rollers and entraining the surrounding water into the inner plume. At the surface, they were advected outward, weakening their rotating motion and increasing in size. In the lower half of the outer plume, most of these eddies were re-entrained into the inner plume. The inner plume fluid farthest from the bubble core was swept downwards by the downdraught before finally being advected horizontally as an intrusion (figure 1*a*). The surface spreading area increased with time until it reached a certain size, at which time the flow remained steady until the ambient stratification began to change (see also Zic *et al.* 1992). This should be compared with the results for a homogeneous fluid where the surface spreading flow induces a circulation cell with a horizontal scale of the order of six times the depth (Goosens 1979; Fanneløp, Hirschberg & Küffer 1991). The strong influence of the eddies on the width of spreading has already been noted by Goosens (1979), Kranenburg (1979), Imberger & Patterson (1990), Asaeda, Imberger & Ikeda (1990) and Zic *et al.* (1992).

The intrusion thickness did not change much until the sidewalls began to influence the propagation of the intrusion; at that stage the intrusions gradually thickened. The intrusion speed was not measured, but the time of influence may be expected to be similar to that found by Maxworthy & Monismith (1988).

At first, both the upper and lower surface of the intrusion remained sharp. However, after the intrusion had reached the sidewalls, the upper layers gradually became mixed into the intrusion flow (see figure 1*b*). As the flow developed, the bottom boundary of the intrusion became well defined with an associated stronger density gradient forming a barrier to the falling water, leading to a further sharpening of the interface. As a result, a homogeneous layer formed at the level of the intrusion, with a strong gradient below it (see figure 1*b*) and a weak transition marking the top.

3.2. *Type* 2 (*moderate gas flow rate and moderate stratification*)

With a decrease in the relative gas flow rate or an increase in the degree of stratification, the flow structure changed to that shown in figure 2(*a*). Above the bubbler a plume formed with a generally rising eddy structure but, upon reaching a certain level, the drag force of the bubbles was insufficient to maintain the negative buoyancy of the entrained heavy water, causing the inner plume to detrain, initiating a downdraught and the formation of an intrusion.

With a decrease in the volume flux of the inner plume, the eddies in the inner plume increased in size relative to the size of the plume and were more ordered. These eddies rose in an alternating pattern which accelerated the mixing within the plume. This feature seemed similar to the difference in the structure of eddies in jets and buoyant plumes (List 1982). When the eddies approached the edge of the inner plume they moved obliquely upwards and toward the outside of the inner plume, entraining the surrounding liquid with a corresponding increase in size and a decrease in density. At the outer edge their negative buoyancy led to a downdraught, forming the outer plume. At the level of neutral buoyancy an outward intrusion formed (figure 2(*a*), the associated mixing causing both upward- and downward-moving water to enter the intrusion (see also McDougall 1978). These intrusions were steady, and the density distribution showed upward transfer of mass (figure 2*b*). At the surface, the inner plume again spread outwards and then plunged once it was arrested by the ambient stratification. The volume flux in this plunging flow formed the upper intrusion; this upper intrusion entrained near-surface water, progressively

homogenizing the upper layer of the tank (figure 2*b*). For a fixed depth, the number of intrusions increased with decreasing gas flow rate and increasing stratification.

3.3. *Type* 3 (*low gas flow rate and strong stratification*)

As the gas flow rate was decreased further or the density stratification increased, the level to which the inner plume could lift the lower water decreased. The resulting flow structure is illustrated in figure 3(*a*). With decreasing gas flow rate, alternating eddies formed within the plume and occupied up to 50% of the inner plume diameter, causing the plume to meander.

As in type 2 flows, the eddies rose in an alternating pattern, entraining the surrounding water. However, eventually they were moved away from the bubble core, becoming larger by further entrainment and less buoyant due to a decreased bubble presence.

The eddies were irregular and increasingly behaved like isolated thermals; collectively they again formed a downdraught annular flow immediately outside the rising inner plume.

At the point of neutral buoyancy some of the water propagated outward in the form of an intrusion resembling type 2 flow, and some recirculated back into the inner plume. The thermals were, however, discrete and so the 'intrusions' were unsteady, poorly defined and confined close to the plume. The net effect was to cause a mass flux through the plume which moved mass from the lower part of the tank to the surface layers (figure 3*b*). This flow was very similar to that observed in the boundary mixing experiments of Ivey & Corcos (1982).

4. Regime analysis

McDougall (1978) proposed two variables, $C\,(=\{4\pi\alpha^2[N^3H_T^4/(Q_0 g H_A/H_T)]\}^{\frac{2}{3}})$ and $M\,(=Q_0 g H_A/(4\pi\alpha^2 H_T^2 u_s^3))$, which were sufficient to non-dimensionalize his integral bubble plume equations. Here, Q_0 is the gas flow rate at the surface, g is the acceleration due to gravity, α is the entrainment coefficient, N is the buoyancy frequency, H_T is the pressure head at the bottom (atmospheric pressure head H_A + water depth H) and u_s is the velocity difference between the bubbles and the liquid. This is called the slip velocity and it is dependent on the bubble size, the surface tension and the air and water viscosities (Clift, Grace & Weber 1978). Schladow (1992) modified C to $P_{HT}\,(=N^3H_T^4/(Q_0 g H_A/H_T))$.

There are thus three independent non-dimensional numbers: M, C and $H/H_T\,(\equiv H_R)$. Together, the values of three numbers determine the plume dynamics. The parameter C denotes the ratio of the potential energy needed to be overcome to lift bottom fluid to the surface to the available bubble buoyancy energy and M is a measure of the effective buoyancy flux of the bubbles as reduced by the bubble slip.

By contrast Asaeda & Imberger (1989) introduced the plume number $\tilde{P}_N$ $(=N^3H^4/(Q_0 g))$. The bubble expansion effect may be included by introducing the bottom volume flux $Q_B\,(=Q_0 H_A/H_T)$ instead of Q_0 and in the present work we shall use the quantity $P_N = N^3H^4/(Q_B g)$. The differences between P_N, $\tilde{P}_N$ and P_{HT} are small, but as will be shown, P_N has the simple interpretation that it represents the ratio of the total depth to the lengthscale of the intrusion spacing.

In the same spirit we use a form of M_H which does not contain H_T, but is defined by $M_H = Q_B g/4\pi\alpha^3 H u_s^3$.

The simple plume value (0.083) was chosen for the entrainment coefficient, α, for calculating M_H (Schladow 1992). Milgram (1983) and Rowe, Poon & Laureshen

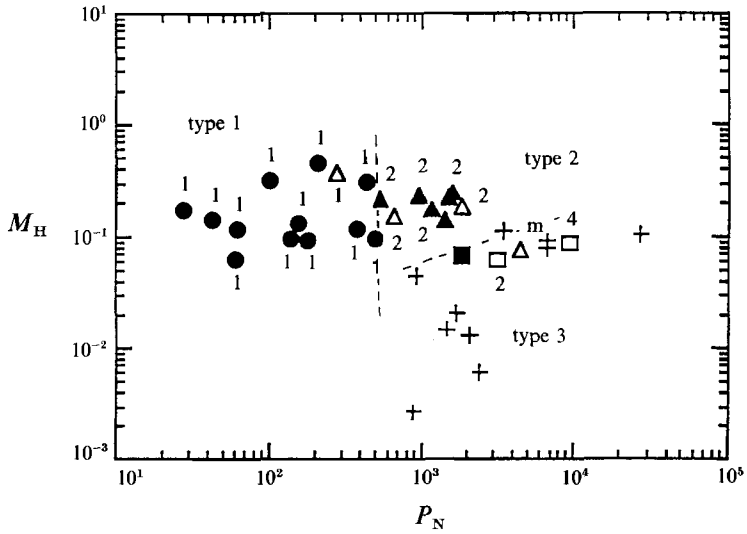

FIGURE 4. Flow patterns in terms of M_H and P_N: ●, type 1; ▲, type 2; +, type 3; □, McDougall (1978); ■, Baines & Leitch (1992); △, Maruyama reservoir experiments (Matsunashi & Miyanaga 1988, 1990). The dashed lines show the boundaries between types. The numbers are the number of intrusions observed, and m represents multiple intrusions (the number is unknown).

(1989) reported that α may vary between 0.04 and 0.12; however, this will not change the fluid motion qualitatively. The available bubble plume data are shown in figure 4 as a function of P_N and M_H. From this figure it is seen that the transition from type 1 to type 2 flows was almost independent of M_H and occurred at a value of P_N approximately equal to 500. The transition to type 3 was less well defined but appeared to occur around $P_N = 2000$; the value was less for small values of M_H and greater for large values of M_H.

The number of intrusions, n, was plotted against P_N (figure 5) and it was found that n increases with increasing P_N according to the relationship:

$$n = \text{integer}[0.22P_N^{\frac{1}{4}} + 1], \tag{1}$$

where the 'integer' function rounds down to the nearest integer. It is worth noting that this implies

$$n = \text{integer}[0.22P_{HT}^{\frac{1}{4}} H_R + 1], \tag{2}$$

consistent with Schladow's (1992) findings.

The relationship (1) implies that the intrusion height, l, is given by

$$l = H/\{\text{integer}[0.22(N^3/Q_B g)^{\frac{1}{4}} H + 1]\} \sim 4.55(Q_B g/N^3)^{\frac{1}{4}}. \tag{3}$$

If we note that, from simple plume analysis (Fischer *et al.* 1979), the velocity scale, u of the inner plume near the base is $O(Q_B g/l)^{\frac{1}{3}}$, then (3) implies that the intrusion distance is fixed by the Ozmidov (1965) length which is determined by the relationship:

$$lN/u = 1. \tag{4}$$

This result is identical to that found by Ivey & Corcos (1982) and Browand, Guyomar & Yoon (1987) for the case of boundary mixing.

Thus, by using the parameters M_H and P_N, the effect on the buoyancy of the compressibility is mostly captured by these numbers and the additional parameter, H_R, may be expected to enter as a scale effect.

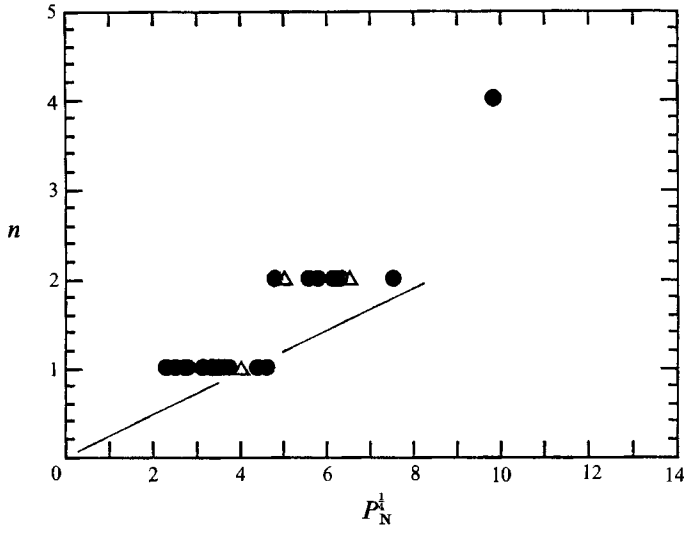

FIGURE 5. The number of intrusions as a function of $P_N^{\frac{1}{4}}$. The solid line shows the relationship given by $n = 0.22P_N^{\frac{1}{4}}$. The hollow triangles are Maruyama reservoir experiments (Matsunashi & Miyanaga 1988).

5. The surface flow

As the inner plume impinged onto the free surface it was turned and spread radially, flowing along the free surface as a negatively buoyant jet until it plunged at a radial distance R (Asaeda *et al.* 1990). An upper bound to R may be obtained with the following argument.

If the intrusions are arranged so that there are an integral number of these over the depth H then the discharge, q, of fluid in the inner plume near the surface is such that

$$q \sim (Q_0 g/h)^{\frac{1}{3}} h^2 = (Q_0 g)^{\frac{1}{3}} h^{\frac{5}{3}}, \tag{5}$$

where h is the intrusion depth near the surface given by $(Q_0 g/N^3)^{\frac{1}{4}}$ and the buoyancy flux near the surface is $Q_0 g$.

The gravitational anomaly between the inner plume water and the ambient water, $\tilde{g}$, is

$$\tilde{g} \sim N^2 h, \tag{6}$$

so that the fall velocity, v, of the outer plume water will scale such that

$$v \sim N^2 h\tau, \tag{7}$$

where τ is the time of travel.

Since the water is spreading radially,

$$\tau \sim R^2 h/q. \tag{8}$$

If it is now assumed that the plume plunges when v equals the radial velocity (q/Rh), then the critical distance becomes

$$R \sim (Q_0 g/N^3)^{\frac{1}{4}}. \tag{9}$$

Using $(Q_0 g/N^3)^{\frac{1}{4}}$ as the non-dimensionalized scale for R yields a data plot as shown in figure 6; the coefficient of the proportionality is thus between 0.7 and 1.5 and the

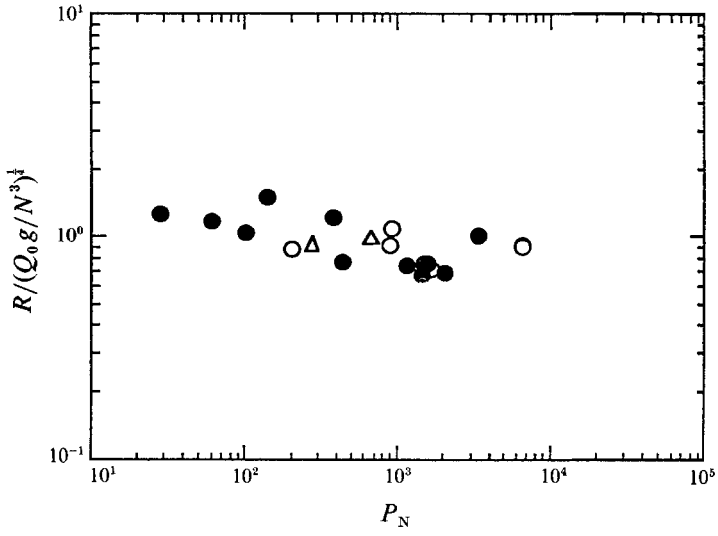

FIGURE 6. The spreading distance along the surface. ●, ceramic bubble-maker experiments; ○, nozzle bubbler experiments; △, Maruyama reservoir experiments (Matsunashi & Miyanaga 1988, 1990).

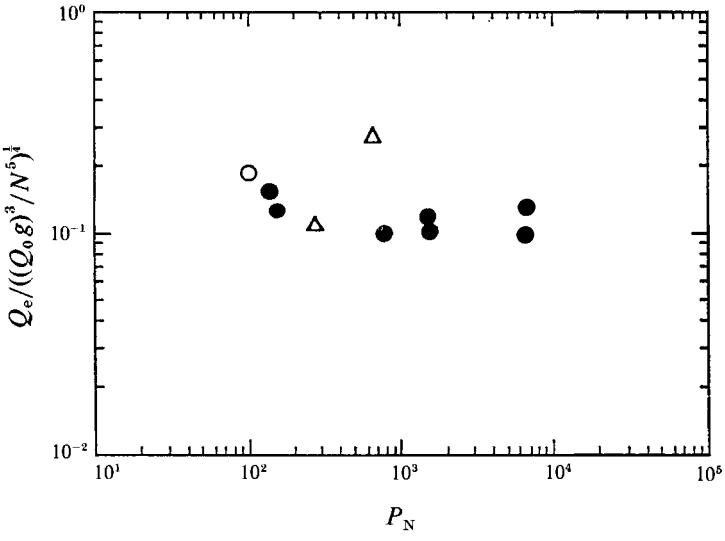

FIGURE 7. The entrainment at the plunge point. ●, ceramic bubble-maker experiments, $H_R \sim 0.055$; ○, $H_R \sim 0.038$; △, field experiments in the Maruyama reservoir (Matsunashi & Miyanaga 1988, 1990).

scaling holds for all experiments, not just the ones with an integral number of intrusions. In the limit N tends to zero (a homogeneous water body; Fanneløp *et al.* 1991), R is bounded by approximately six times the depth of the water body.

At the plunge point, the falling water mass entrained ambient water which reduced the density anomaly (Asaeda, Nakai & Tamai 1989; Zic & Stefan 1990, p. 128). This had a strong influence on the downdraught flow. The total entrainment between the surface and the highest intrusion, Q_e, is shown in figure 7 non-dimensionalized by the inner plume flow $q \sim ((Q_0 g)^3/N^5)^{\frac{1}{4}}$. The quantity Q_e was

obtained by noting the rate of change of the isopycnal heights from two distribution measurements and dye photographs. From figure 7, it follows that

$$Q_e = 0.1((Q_0 g)^3/N^5)^{\frac{1}{4}}, \tag{10}$$

implying that the rate of entrainment scales with the volume flux of the inner plume.

6. Analysis

6.1. *The model equations*

The observations described above lead to a 'partial double-plume model' structure in which upward momentum is confined to an inner plume, while the detrained water forms the outer downward-moving annular plume (see figure 8). This model is different to the one proposed by McDougall (1978) who postulated that the bubble core and the surrounding rising liquid form two distinct flow regions; by contrast, these two flows form the inner plume in the present model; he did not allow for a downdraught. The annular downdraught is assumed to fall down to the neutral buoyancy level, then spread out horizontally as an intrusion. The inner plume only entrains the ambient water below the level of the intrusion. Above this level, there is exchange between the rising inner plume and the falling outer plume. In order to describe the motion of the partial double-plume structure, it was necessary to make some assumptions about the rate of the interaction between the outer and inner plumes. The usual entrainment assumption must be generalized. Following Morton (1962), it is assumed that the supply of energy to the turbulence in the inner plume arises from the difference in velocities between the inner and the outer plumes, whereas the turbulence in the outer plume is the result of the outer shear layer dynamics. Thus, we may expect the entrainment velocity of outer plume fluid into the inner plume to be proportional to the velocity difference between the inner and the outer plumes, but the rate of entrainment of the inner plume into the outer plume to depend only on the outer plume velocity.

Assuming a top-hat velocity and buoyancy profile, a constant horizontal pressure surface and negligible turbulent transport lead to integral equations for the inner core as follows:

$$\mathrm{d}(a^2u)/\mathrm{d}z = 2a\beta(u-v)+2a\gamma v, \tag{11}$$

$$\mathrm{d}(a^2u^2)/\mathrm{d}z = a^2g'+2a\beta v(u-v)+2a\gamma uv, \tag{12}$$

$$\mathrm{d}(a^2ug')/\mathrm{d}z = (a^2ug/\bar{\rho})(\mathrm{d}\rho_a/\mathrm{d}z)-2a\beta(u-v)g''+2a\gamma v\tilde{g}+\mathrm{d}(a^2guF)/\mathrm{d}z; \tag{13}$$

and for the outer plume:

$$\mathrm{d}((b^2-a^2)v)/\mathrm{d}z = -2a\beta(u-v)-2a\gamma v-2b\alpha v, \tag{14}$$

$$\mathrm{d}((b^2-a^2)v^2)/\mathrm{d}z = -(b^2-a^2)g''-2a\beta v(u-v)-2a\gamma uv, \tag{15}$$

$$\mathrm{d}((b^2-a^2)vg'')/\mathrm{d}z = -[(b^2-a^2)vg/\bar{\rho}](\mathrm{d}\rho_a/\mathrm{d}z)-2a\beta(u-v)g''+2a\gamma v\tilde{g}, \tag{16}$$

where a and b are the inner and outer plume radii, u and v are the inner and outer plume velocities, $g' = g(\rho_a-\rho_i)/\bar{\rho}$, $g'' = g(\rho_o-\rho_a)/\bar{\rho}$, $\tilde{g} = g'-gF$, where subscript i denotes the inner plume, subscript o the outer plume, and subscript a the ambient environment, and F is the total fraction occupied by gas, $\bar{\rho}$ is the reference density, α, β, γ are the entrainment coefficients from the environment to the outer plume, from the outer to the inner plume, and from the inner to the outer plume respectively and z is the vertical upward coordinate.

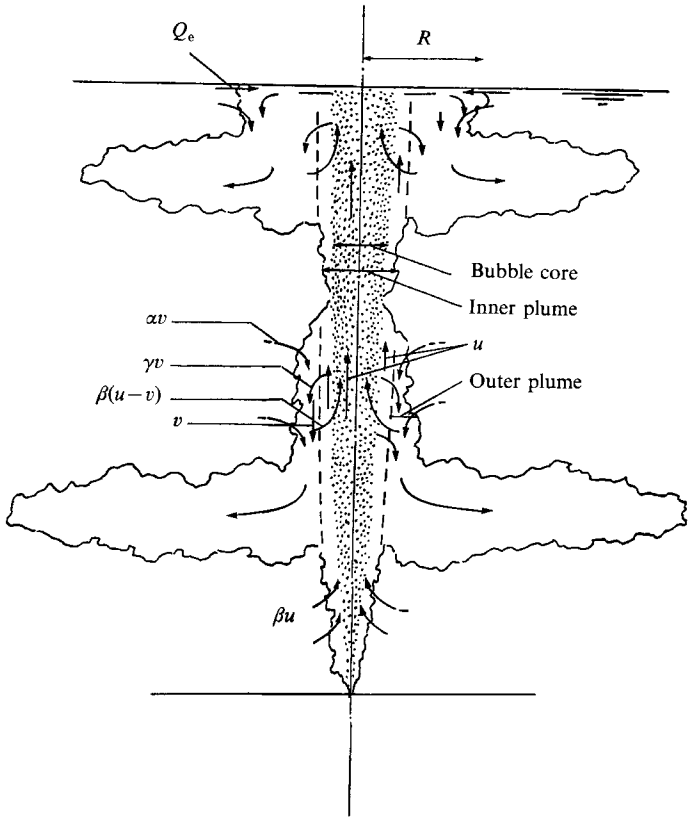

FIGURE 8. Diagram of the double-plume model.

These equations may be non-dimensionalized by

$$a = 2\alpha HA, \quad b = 2\alpha HB, \quad u = u_s M_H^{\frac{1}{3}} U, \quad v = u_s M_H^{\frac{1}{3}} V,$$
$$g' = u_s^2 M_H^{\frac{2}{3}} G'/H, \quad g'' = u_s^2 M_H^{\frac{2}{3}} G''/H, \quad S^2 = B^2 - A^2, \quad z = Hx,$$
$$\beta = \beta/\alpha, \quad \Gamma = \gamma/\alpha, \quad \tilde{G} = G' - 1/[(1-xH_R)(U+M_H^{-\frac{1}{3}})\tilde{A}^2],$$

where the z coordinate has been non-dimensionalized with respect to H, and $\tilde{A}$ is the bubble core radius.

Normally, $\tilde{A}$ depends not only on the liquid flow pattern but also on the bubble characteristics. The value used was the smaller of the calculated $\tilde{A}\,(=A\lambda)$ and the one for a homogeneous liquid ($\tilde{A} = 0.1(x+0.05)K^{\frac{3}{5}}/\alpha$). Here λ is the ratio of the bubble core radius to the inner plume radius ($= 1.2[W/(71+W)]$), where $W = [\bar{\rho}(Q_0^4 g^3)^{\frac{1}{5}}/\sigma]^{\frac{1}{2}}$ (Rowe *et al.* 1989) σ is the surface tension coefficient, and $K = \tanh[(gQ_0/H_A)^{\frac{1}{3}}/u_s]$ (Kobus 1973, p. 168). The calculated inner plume radius agreed well with the results of McDougall's (1978) analysis. Then,

$$\mathrm{d}(A^2U)/\mathrm{d}x = \beta A(U-V) + \Gamma AV, \tag{17}$$
$$\mathrm{d}(A^2U^2)/\mathrm{d}x = A^2G' + \beta AV(U-V) + \Gamma AUV, \tag{18}$$
$$\frac{\mathrm{d}(A^2UG')}{\mathrm{d}x} = -A^2UC_H - \beta AG''(U-V) + \Gamma AV_{\tilde{G}} + \frac{\mathrm{d}}{\mathrm{d}x}\left[\frac{A^2U}{\tilde{A}^2(1-xH_R)(U+M_H^{-\frac{1}{3}})}\right], \tag{19}$$
$$\mathrm{d}(S^2V)/\mathrm{d}x = -\beta A(U-V) - \Gamma AV - BV, \tag{20}$$
$$\mathrm{d}(S^2V^2)/\mathrm{d}x = -S^2G'' - \beta AV(U-V) - \Gamma AUV, \tag{21}$$

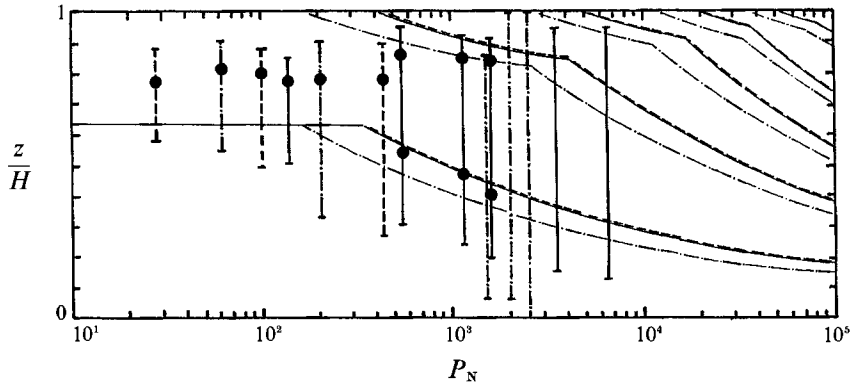

FIGURE 9. Intrusion positions within H. Vertical lines show the region where intrusions form; ——, ceramic bubbler experiments ($0.09 < M_H < 0.31$), and $H_R \sim 0.055$; – – – –, ceramic bubbler experiments, and $H_R \sim 0.038$; –·–·–, nozzle bubbler experiments ($0.01 < M_H < 0.11$), and $H_R \sim 0.055$; ●, experimental results for intrusion positions. Oblique curves are calculated intrusion positions: ——, $M_H = 0.2$, $H_R = 0.055$; – – – –, $M_H = 0.2$, $H_R = 0.038$; –·–·–, $M_H = 0.02$, $H_R = 0.055$.

and
$$\mathrm{d}(S^2VG'')/\mathrm{d}x = S^2VC_H - \beta AG''(U-V) + \Gamma AV\tilde{G}, \tag{22}$$
where $C_H = (4\pi)^{\frac{2}{3}}\alpha^{\frac{4}{3}}P_N^{\frac{2}{3}}$.

Equations (17)–(22) were solved iteratively using a Runge–Kutta procedure. First, the inner plume equations were solved with the starting conditions detailed in §6.2 below. The integrations were carried out to the point where the upward momentum was zero. The outer plume was then integrated downwards from the inner-plume exit point to the level of neutral buoyancy. During this downward integration, the values used for A, U, and G' at each level were those derived by the previous integration up the inner plume. This process was repeated until the solution had converged; the criterion of the convergence was defined such that the difference in the buoyancy flux of the inner plume became less than 1% from the former integration.

For cases where the inner-plume exit point was below the water surface, the procedure was repeated until the free surface was reached. At the free surface, the rising flow was used to feed a spreading radial plume with the entrainment (10) added to the flow before it was routed downwards with an initial radius given by (9). The coefficient, Γ, was given a pure plume value and β was adjusted to a value of 0.5 which gave the best comparison with the experimental data; a pure jet entrainment would yield a value of 0.4 (Fischer *et al.* 1979).

6.2. *Starting conditions*

Close to the bubble source no outer plume exists so that the single-plume analysis of McDougall (1978) was used to initiate the integration, and the simple perturbation analysis was used to find a series solution to (17), (18), (20) and (21):
$$A = x[0.6 + 0.01719M_H^{-\frac{1}{3}}x^{\frac{1}{3}} - 0.002527M_H^{-\frac{2}{3}}x^{\frac{2}{3}} + x(-0.04609 + 0.000031M_H^{-1}) + \ldots], \tag{23}$$
$$U = x^{-\frac{1}{3}}[1.609 - 0.3195M_H^{-\frac{1}{3}}x^{\frac{1}{3}} + 0.06693M_H^{-\frac{2}{3}}x^{\frac{2}{3}} + x(0.4536 - 0.0105M_H^{-1}) + \ldots]. \tag{24}$$
The initial value of buoyancy flux A^2UG' can be obtained as
$$A^2UG' = -C_H A^2Ux + A^2U/[\tilde{A}^2(1 - xH_R)(U + M_H^{-\frac{1}{3}})]. \tag{25}$$
The assumption that the inner plume corresponds to the upward momentum core

makes it impossible to differentiate between the height where the velocity of the surrounding rising liquid becomes zero and the height where the total average of the inner plume velocity becomes zero. However, as these heights are close together (McDougall 1978), we assumed that they were the same.

The starting conditions of the outer downward plume were determined as follows. First, the volume flux condition was assumed to be given by

$$S^2V = -A^2U. \tag{26}$$

Then, from (21), the initial momentum flux is given by

$$S^2V^2 = S^2G''(\tilde{x}-x) \quad \text{for small} \quad (\tilde{x}-x), \tag{27}$$

where $\tilde{x}$ is the starting level of the outer plume.

From (19) and (22), the buoyancy flux condition was obtained as follows:

$$S^2VG'' = A^2UG' - UA^2/[(1-xH_R)(U+M_H^{-\frac{1}{3}})\tilde{A}^2]. \tag{28}$$

The next inner plume starts with the radius which is assumed as the bubble core radius in homogeneous water (see §6.1). At the small starting value of $x-\tilde{x}$, the stratification of the environment had a negligible effect so that the buoyancy of the inner plume was entirely due to the bubbles ($\tilde{G}=0$). Therefore, from (18),

$$U^2 = (x-\tilde{x})/[(1-xH_R)(U+M_H^{-\frac{1}{3}})\tilde{A}^2] \quad \text{for} \quad \tilde{A} \gg (x-\tilde{x}). \tag{29}$$

The starting buoyancy flux is given by (25).

7. Position of intrusions

Figure 9 shows the levels and the vertical extent of the intrusions from the experiments and the intrusion levels as predicted by the model. These results show that, with increasing H_R, more intrusions form, and the level of the lowest intrusion is lowered.

With increasing P_N or decreasing M_H, and constant H_R, again more intrusions form and the lowest intrusion level decreases and the highest intrusion is higher. This may be explained by noting that with decreasing gas flow rate, relatively to the stratification, positive momentum decreases faster and detrainment occurs earlier. The model also predicted that the intrusion spacing becomes slightly smaller with increasing height. This is because the inner plume size increases gradually with height, which increases the negative buoyancy force per unit height, slowing the plume more rapidly; heavier water is detrained earlier and forms a larger number of intrusions. This means that (3) must be interpreted as an average intrusion height.

The intrusion thickness also scales with $(Q_B g/N^3)^{\frac{1}{4}}$ (see Lemckert & Imberger 1992*b*) and from the present observations the thickness occupied only about 15% of the intrusion spacing for type 2 flows. The one-dimensional model may thus be expected to yield an adequate representation of the plume behaviour.

8. Energy conversion

The most important factor to be considered in the design of a bubble plume scheme for the destratification of a reservoir is how much of the energy supplied by the bubbles is converted to potential energy of the density distribution. If ΔE is the change of potential energy in time Δt, then an efficiency, η, may be defined by

$$\eta = \Delta E/[\bar{\rho}Q_0 g H_A \ln(1+H/H_A)\Delta t], \tag{30}$$

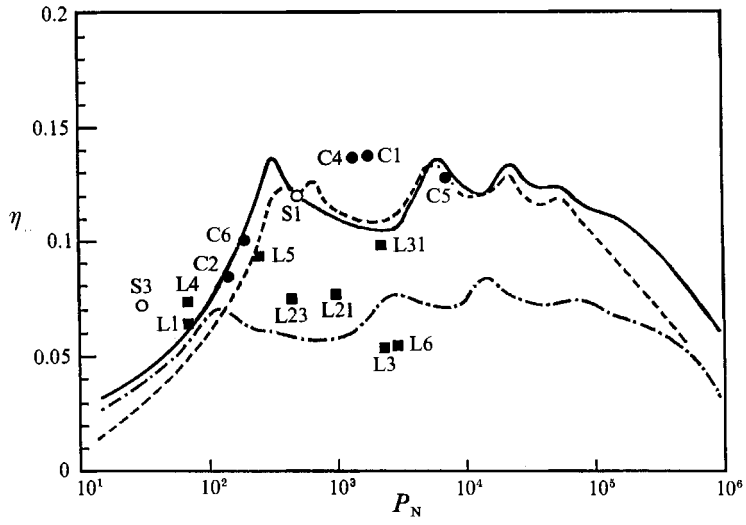

FIGURE 10. Efficiency as a function of P_N. Symbols are experimental results (table 1): ●, $0.09 < M_H < 0.23$ (ceramic bubbler), $H_R \sim 0.055$; ○, $0.17 < M_H < 0.3$, $H_R \sim 0.038$; ■, $0.006 < M < 0.11$ (nozzle bubbler), $H_R \sim 0.055$. Curves are the calculated results: ——, $M_H = 0.2$, $H_R = 0.055$; –·–·–, $M_H = 0.02$, $H_R = 0.055$; – – – –, $M_H = 0.2$, $H_R = 0.38$.

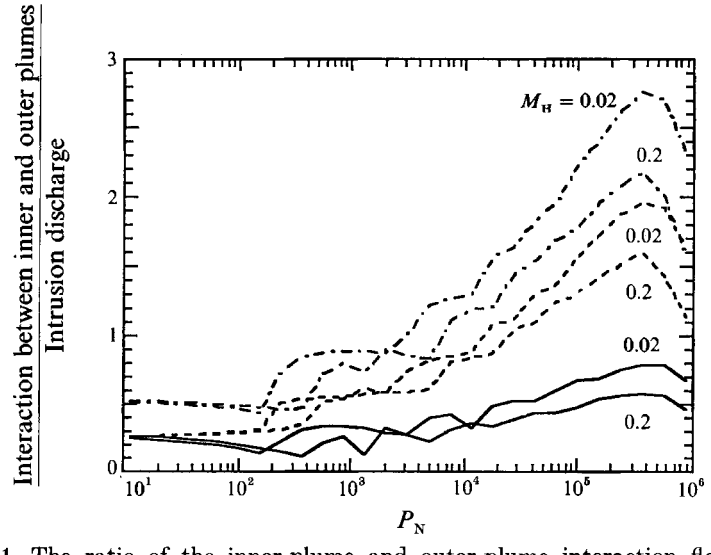

FIGURE 11. The ratio of the inner-plume and outer-plume interaction flow to the intrusion discharge. $H_R = 0.055$: –·–·–, the entrained flow divided by the intrusion discharge; – – – –, the detrained flow divided by the intrusion discharge; ——, the difference between the entrained and the detrained flow divided by the intrusion discharge.

since $\bar{\rho} Q_0 g H_A \ln(1 + H/H_A)$ is the work required to isothermally compress air from atmospheric pressure to a pressure at depth H at a rate of Q_0.

Figure 10 shows the efficiency as a function of P_N immediately after turning on the bubbler. The efficiency generally decreased with time, but increased rapidly with P_N as the flow changed from type 1 to type 2, and decreased gradually from type 2 to type 3. In general, the calculated results agree well with the experimental results.

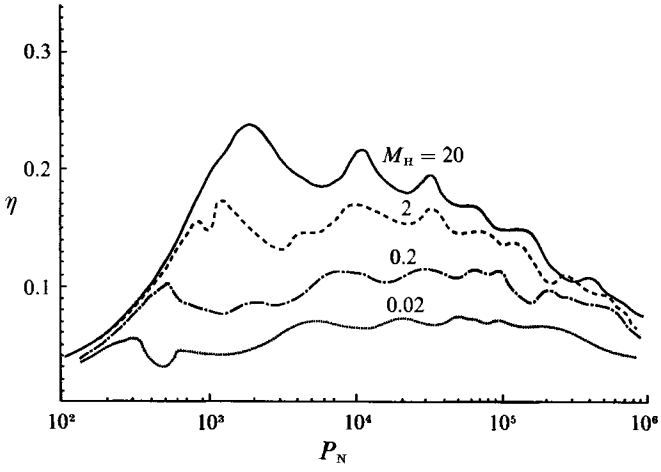

FIGURE 12. The variation of the plume efficiency, η, as a function of P_N for different values of M_H for $H_R = 0.5$. Results in figures 12, 13 and 14 are all from the numerical model.

The small efficiencies at small values of P_N are due to an over supply of energy into a weak stratification; most of the energy is dissipated in turbulence. As P_N approaches a value of around 500, the fluid travel time approximately equals N^{-1} (Froude number order one) and the efficiency peaks; this is well documented in other papers (see Imberger & Ivey 1993). Since the entrainment at the surface is higher with smaller P_N, the efficiency again decreases as P_N is increased. In addition, with increasing P_N, most of the water detrained at the higher level is re-entrained at the lower level, again decreasing the efficiency. This mechanism is shown in figure 11, where the calculated ratio of the amount of fluid recirculating between the outer and inner plumes is shown; the minimum corresponds to the point where the efficiency is highest. With decreasing M_H, this ratio increases, indicating the increase in the recirculating flow and the decrease in the intrusion discharge.

The numerical model was used to investigate the variation of the efficiency over a wide range of values of P_N and M_H; for $H_R = 0.5$ this is shown in figure 12. From these results it is clearly seen that the peak efficiency is a strong function of M_H and attains values considerably higher than those generally assumed in bubble plume designs (Davis 1980). The local peaks arise whenever the plume has an integral number of intrusions for the particular depth. The sawtooth nature of the efficiency curves was previously noticed by Schladow (1992) who used a single-core numerical model.

The value of P_N at maximum efficiency, P_N^*, for different values of M_H and H_R is shown in figure 13 by dashed lines. The solid lines are introduced as a design aid and are discussed below. The variation is almost linear on this log–log plot and is closely approximated by

$$P_N^* = 10^{[0.16 \log_{10} M_H + (2.5 + 1.4 H_R + 0.65 H_R^2)]}. \tag{31}$$

The dependence of the maximum efficiency on M_H and H_R is now well defined and is shown in figure 14; the maximum efficiency increases with increasing H_R and M_H.

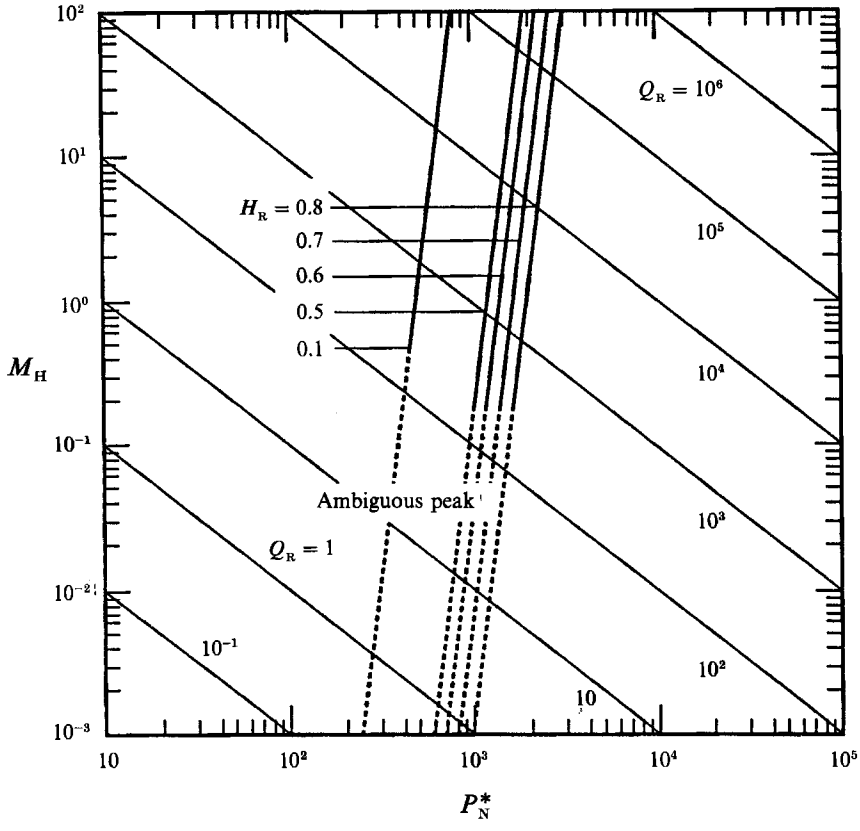

FIGURE 13. P_N^*, the values of P_N which correspond to the maximum efficiency, as a function of M_H and different values of H_R (dashed lines). For $M_H < 2 \times 10^{-1}$ the maximum efficiency was not well defined. The definitions of the variables are given in the text, but since this diagram is the key figure for design purposes we define them again here: $H_R = H/H_T$; $Q_R = Q_p/Q_M$; $P_N^* = N^3H^4/(Q_B^* g)$; $M_H^* = Q_B^* g/(4\pi\alpha^3 H u_s^3)$; $Q_p = N^3H^4/g$; $Q_M = (4\pi\alpha^2 H u_s^3)/g$. The solid lines show lines of constant Q_R.

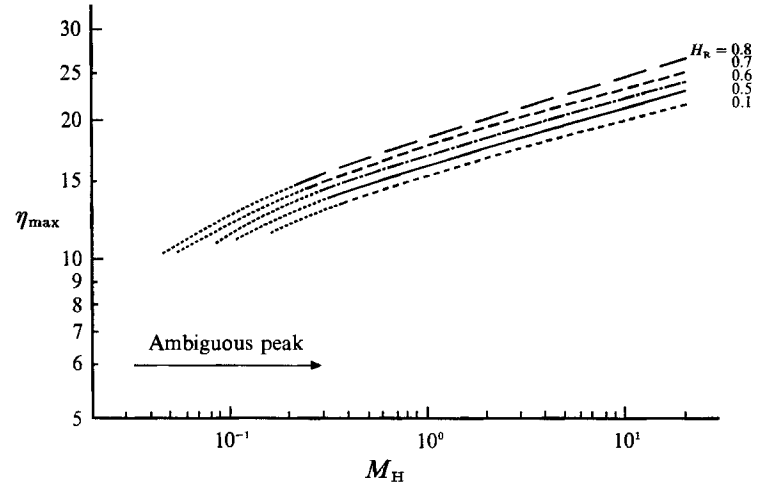

FIGURE 14. The maximum efficiency, η_{max}, as a function of M_H for different values of H_R. For values of M_H less than about 2×10^{-1}, the maximum efficiency was not well defined.

9. Discussion

The design of a destratification bubble plume system is thus particularly simple. From a knowledge of the reservoir depth, H, we can calculate $H_R (= H/H_T)$. The bubble size determines the bubble slip velocity u_s, and for a 1.5 mm diameter air hole (now relatively standard) a reasonable value for u_s is 0.3 m s^{-1} (Kobus 1973, p. 168; Goosens & Van Pagee 1977; Milgram 1983). With these values it is now possible to find the appropriate value of the bottom gas flow rate, Q_B^*, that satisfies the relationships given in figure 13; i.e. that Q_B^* which yields a flow with maximum efficiency.

This is most easily done by introducing two additional flow rates:

$$Q_M = 4\pi\alpha^2 H u_s^3/g \tag{32}$$

and

$$Q_p = N^3 H^4/g, \tag{33}$$

so that

$$M_H^* = Q_B^*/Q_M \tag{34}$$

and

$$P_N^* = Q_p/Q_B^*. \tag{35}$$

Eliminating Q_B^* from (34) and (35) leads to the relationship

$$M_H^* = Q_p/(Q_M P_N^*), \tag{36}$$

and substituting this into (31) yields the required relationship:

$$P_N^* = 10^{[0.16\log_{10}(Q_p/Q_M)+(2.1+1.2H_R-0.55H_R^2)]}. \tag{37}$$

A graphical procedure to arrive at a solution of (37) is given in figure 13. Once H_R and Q_R $(= Q_p/Q_M)$ are known, the P_N^* may be obtained from figure 13. The corresponding flow rate, per diffuser port, is then given by

$$Q_B^* = H^4 N^3/(P_N^* g). \tag{38}$$

It is noteworthy, by comparison with (3), that this corresponds to a flow pattern in which the first intrusion is well established and the second is just beginning to form.

Now if it is desired to destratify the reservoir in a period, T, then the number, m, of ports required will be given by

$$m = \Omega/(TQ_I), \tag{39}$$

where Ω is the volume of the reservoir and Q_I is the total volume flux of a single plume structure. From the present data set it was not possible to evaluate Q_I as the tank was too small. However, recently Lemckert & Imberger (1992*a*), using field data, have determined that

$$Q_I = 0.74(Q_B g)^{\frac{3}{4}}/N^{\frac{1}{4}} M_H^{0.11}. \tag{40}$$

The flow rate Q_I, given by (40), was tested by these authors against a wide range of conditions.

The spacing of the ports should be at least 2–4 times the radius (9) and the compressor power requirement without head losses, P, also follows immediately from the value of Q_B^* and is given by

$$P = m\bar{\rho} Q_B^* H_T \ln(1 + H/H_A), \tag{41}$$

where $\bar{\rho}$ = density of water.

10. Conclusions

The structure of bubble plumes in a linear stratification was investigated. Bubble plumes detrain fluid outwards; the detrained water forms various types of intrusions, depending on the relation between the intensity of the stratification and the gas flow rate. The height between intrusions and the plunge point radius were shown to scale with the Ozmidov length and the plunge point entrainment scaled with the inner volume flux. The efficiency of energy conversion was shown to reach a maximum at a particular value of P_N dependent on the value of M_H and H_R.

In general it was shown that the bubble plume behaviour was captured by the values of the parameters M_H, P_N and H_R; this realization allowed the formulation of a simple design procedure for bubble plume destratification systems.

The authors wish to thank Drs J. C. Patterson, G. N. Ivey, J. Taylor, S. W. Armfield, S. G. Schladow and K. Zic, and C. J. Lemckert for their useful discussions; W. Deugd for his technical assistance; H. Ikeda and M. Asaeda for their assistance in the experiments. The first author was supported by the University of Western Australia through the Mosey Scholarship Scheme, the Centre for Environmental Fluid Dynamics and the Kajima Foundation. Experimental work was also financially supported by the Sydney Water Board and the Department of Water Resources of New South Wales.

REFERENCES

Asaeda, T. & Imberger, J. 1989 Behaviours of bubble plumes in a linear stratification. *Proc. JSCE* **411**, 55–62 (in Japanese).

Asaeda, T., Imberger, J. & Ikeda, H. 1990 Bubble plume behaviours in two-layered environments. *Res. Rep. Dept Found. Engng & Const. Engng, Saitama Univ.*, vol. 20, pp. 19–32.

Asaeda, T., Nakai, M. & Tamai, N. 1989 Spreading rate of dense jet impinging on the free surface. *Proc. JSCE* **411**, 109–116 (in Japanese).

Baines, W. D. & Leitch, A. M. 1992 Destruction of stratification by a bubble plume. *J. Hydraul. Engng ASCE* **118**, 559–577.

Browand, F. K., Guyomar, D. & Yoon, S. C. 1987 The behavior of a turbulent front in a stratified fluid: Experiments with an oscillating grid. *J. Geophys. Res.* **92**, 5329–5341.

Bulson, P. S. 1961 Current production by an air curtain in deep water. *Dock Harbour Authority* **42**, 15–22.

Cheung, F. B. & Epstein, M. 1987 Two-phase gas bubble–liquid boundary layer flow along vertical and inclined surface. *Nucl. Engng Design* **99**, 93–100.

Clift, R., Grace, J. R. & Weber, M. E. 1978 *Bubbles, Drops and Particles*. Academic.

Davis, J. M. 1980 Destratification of reservoirs – a design approach for perforated-pipe compressed-air systems. *Water Services* **84**, 497–504.

Ditmars, J. D. & Cederwall, K. 1974 Analysis of air-bubble plumes. In *Proc. 14th Conf. Coastal Engng, Copenhagen*, Ch. 128, pp. 2209–2226. ASCE.

Fanneløp, T. K., Hirschberg, S. & Küffer, J. 1991 Surface current and recirculating cells generated by bubble curtains and jets. *J. Fluid Mech.* **229**, 629–657.

Fischer, H. B., List, E. G., Koh, R. C. Y., Imberger, J. & Brooks, N. H. 1979 *Mixing in Inland and Coastal Waters*. Academic.

Goosens, L. H. J. 1979 Reservoir destratification with bubble columns. Thesis, Delft University. The Netherlands.

Goosens, L. H. J. & Van Pagee, J. A. 1977 Modelling of the near field due to air injection in big reservoirs. *Proc. 17th Cong. IAHR*, vol. 1, pp. 551–560.

HEAD, M. J. 1983 The use of miniature four-electrode conductivity probes for high resolution measurement of turbulent density or temperature variations in salt-stratified water flows. Ph.D. dissertation, University of California, San Diego.

HUSSAIN, N. A. & NARANG, B. S. 1984 Simplified analysis of air-bubble plumes in moderately stratified environments. *Trans. ASME* C: **106**, 543–551.

IMBERGER, J. & IVEY, G. N. 1993 Boundary mixing in stratified reservoirs. *J. Fluid Mech.* **248**, 477–491.

IMBERGER, J. & PATTERSON, J. C. 1990 Physical limnology. *Adv. Appl. Mech.* **27**, 303–475.

IVEY, G. N. & CORCOS, G. M. 1982 Boundary mixing in a stratified fluid. *J. Fluid Mech.* **121**, 1–26.

KOBUS, H. E. 1968 Analysis of the flow induced by an air-bubble system. In *Proc. 11th Conf. Coastal Engng, London*, pp. 1016–1031. ASCE.

KOBUS, H. 1973 *Wasser und Abwasser*. Erich Schmidt.

KRANENBURG, C. 1979 Destratification of lakes using bubble columns. *J. Hydraul. Engng, Proc. ASCE* **105** (HY4), 333–349.

LEMCKERT, C. J. & IMBERGER, J. 1992*a* Energetic bubble plumes in arbitrary stratification. *J. Hydraul. Engng, ASCE* (in press).

LEMCKERT, C. J. & IMBERGER, J. 1992*b* Axisymmetric intrusive gravity currents in linearly stratified fluids. *J. Hydraul. Engng, ASCE* (in press).

LIST, E. J. 1982 Mechanism of turbulent jets and plumes. In *Turbulent Buoyant Jets and Plumes* (ed. W. Rodi), pp. 1–62. Pergamon.

MATSUNASHI, G. & MIYANAGA, Y. 1988 Basic study of air bubble plume used for measure against water quality. *Abiko Lab. Rep.* U87066, p. 39 (in Japanese).

MATSUNASHI, G. & MIYANAGA, Y. 1990 A field study on the characteristics of air bubble plume in a reservoir. *J. Hydrosci. Hydraul. Engng, Proc. JSCE* **9**, 65–78.

MAXWORTHY, T. & MONISMITH, S. G. 1988 Differential mixing in a stratified fluid. *J. Fluid Mech.* **189**, 571–598.

MCDOUGALL, T. J. 1978 Bubble plumes in stratified environments. *J. Fluid Mech.* **85**, 655–672.

MILGRAM, J. H. 1983 Mean flow in round bubble plumes. *J. Fluid Mech.* **133**, 345–376.

MORTON, B. R. 1962 Coaxial turbulent jets. *Intl J. Heat Mass Transfer* **5**, 955–965.

OZMIDOV, R. V. 1965 On the turbulent exchange in a stably stratified ocean. *Izv. Acad. Sci. USSR, Atmos. Ocean Phys.* **1**, 493–497. (Engl. Transl.)

ROWE, R. D., POON, J. Y. C. & LAURESHEN, C. J. 1989 A simple method for predicting bubble plume properties. *Proc. 23rd Intl Assoc. Hydr. Res. Ottawa*, D-23-30.

SCHLADOW, S. G. 1992 Bubble plume dynamics in a stratified medium and the implications for water quality amelioration in lakes. *Wat. Resour. Res.* **28**, 313–321.

SUN, T. Y. & FAETH, G. M. 1986 Structure of turbulent bubbly jets – 1. Methods and centreline properties. *Intl J. Multiphase Flow* **12**, 99–114.

TACKE, K. H., SCHUBERT, H. G., WEBER, D. J. & SCHWERDTFEGER, K. 1985 Characteristics of round vertical gas bubble jets. *Metall. Trans.* B **16**, 263–275.

WILKINSON, D. L. 1979 Two-dimensional bubble plumes. *J. Hydraul. Div.* ASCE **105** (HY2), 139–154.

ZIC, K. & STEPHAN, H. G. 1990 Analysis and simulation of mixing of stratified lakes or reservoirs by air bubble plumes. *Project Rep.* 305, St Anthony Falls Hydraulic Laboratory.

ZIC, K. & STEPHAN, H. G. & ELLIS, C. 1992 Laboratory study of bubble plume destratification. *J. Hydraul. Res.* **30**, 7–27.